Automated Deployment of an Underwater Tether Equipped with a Compliant Buoy–Ballast System for Remotely Operated Vehicle Intervention

Ornella Tortorici, Charly Péraud, Cédric Anthierens, Vincent Hugel

Journal of
Marine Science and Engineering

MDPI

Article

Automated Deployment of an Underwater Tether Equipped with a Compliant Buoy–Ballast System for Remotely Operated Vehicle Intervention

Ornella Tortorici [1], Charly Péraud [2], Cédric Anthierens [2] and Vincent Hugel [2,*]

[1] Institute for Mechatronics in Mechanics, 21073 Hamburg, Germany; tortorici.ornella@gmail.com
[2] Université de Toulon, COSMER, 83041 Toulon, France; charly-peraud@etud.univ-tln.fr (C.P.); cedric.anthierens@univ-tln.fr (C.A.)
* Correspondence: vincent.hugel@univ-tln.fr

Abstract: Underwater remotely operated vehicles (ROVs) are linked to the surface through a tether that is usually controlled by a human operator. The length of the tether being deployed in the water in real time is a critical determinant of the success of the mission, and the problems of entanglement and cable stretching must be anticipated to the greatest possible extent. This paper describes a low-cost and setup-friendly solution for managing the length of a neutrally buoyant tether using a balanced buoy–ballast system implemented on the part of the tether proximal to the ROV. Embedded in the system is a curvature sensor that helps to control the cable feeder on the surface. This represents a useful solution for smoothing tether movements and to damp external disturbances. The results of experiments carried out in water tanks demonstrate the benefits of this solution in allowing the cable to maintain a semi-stretched shape while ensuring that the ROV avoids being pulled by the cable. Possible applications for a surface vehicle linked to an ROV through a tether equipped with this compliant buoy–ballast system include exploration or cartography missions in shallow waters.

Keywords: underwater robotics; tethered robot; buoy–ballast system; length control

Citation: Tortorici, O.; Péraud, C.; Anthierens, C.; Hugel, V. Automated Deployment of an Underwater Tether Equipped with a Compliant Buoy–Ballast System for Remotely Operated Vehicle Intervention. *J. Mar. Sci. Eng.* **2024**, *1*, 0. https://doi.org/

Received: 10 January 2024
Revised: 31 January 2024
Accepted: 1 February 2024
Published:

1. Introduction

Most underwater exploration and inspection tasks are achieved by remotely operated vehicles (ROVs), whose maneuverability and reliability are at the heart of a mission's success [1,2]. Maintenance missions include the inspection of ship hulls, pontoons, offshore wind farms, oil platforms, risers, and seabed pipelines as well as all artificial sensing structures integrated in the oceans for monitoring the seas or conducting physics experiments, such as the neutrino telescope in the Mediterranean Sea [3]. ROVs are linked to a surface control vessel by a tether that can transmit data and even supply power if necessary [4,5]. However, the tether is likely to apply undesirable forces on the ROV through its attachment point [6,7], which can affect the ROV's mobility and its planned trajectory while increasing power consumption [8–11]. Tether constraints are even more important for small and less powerful ROVs, which are also widely used in shallow waters. A slack, passive tether increases the risk of entanglement and seabed drag, resulting in premature wear [12–14]. To take advantage of the cables linked to underwater robots, a control system for varying cable length is required.

One of the main challenges in underwater robotics is to provide robots with more navigation autonomy and maneuverability, whereas tether deployment remains under the control of a skilled human operator. In the literature, there exist three main solutions for the management of subsea tethers, namely involving tether customization/instrumentation, use of surface winches, or use of an underwater tether management system (TMS), which can be implemented by an auxiliary robot.

Tethers are often customized by buoys and ballasts to change their buoyancy, shape, or behavior [7,15,16]. Such systems are passive, and their positive impact on cable management is limited when they are not used in conjunction with active length control. Cables can also be fitted with external or internal sensors to monitor their behavior and shape, e.g., taking measurements at several specific nodes along the cable through inertial or tension sensors [7,17] or continuously along the entire cable through embedded fiber optic solutions [18–20]. The first solution generates an irregular shape, whereas the second can be very expensive. Surface winches are used for cable winding and unwinding and are often operated either manually or simply based on cable tension [21,22]. They are commonly placed on the surface vessel, but they can also be embedded on the ROV itself, which involves technological challenges [15]. tether management systems (TMSs) are widely used for deep water systems [1,23–25]. Located between the surface and the ROV, they manage the portion of the cable connected to the ROV. They are usually combined with a depressor weight to limit the transmission of heave motion from the surface vessel to the ROV via the tether. An auxiliary ROV can also play the role of a TMS [2]. It can be remotely controlled by an operator or automatically manage the shape of passive weighing cables [26]. However, this solution introduces the potential risk of collision between the robots.

This paper presents a mechatronic solution for automating the deployment of a tether that links a remotely operated vehicle to the surface while limiting unwanted disturbances to the ROV.

This solution is designed to be installed easily on an existing neutrally buoyant and lightweight cable. It is a low-cost solution that consists of combining two buoys and a ballast located between the buoys, and a flex sensor is mounted at the ballast. The buoy–ballast system is also built to be neutrally buoyant and behave as a compliant system in preventing the ROV from being pulled by the cable and enabling active cable management using the flex sensor. Unlike most existing solutions designed for weighing cables, the system presented in this article is original and suitable for neutrally buoyant cables, which do not carry energy. Alternative solutions for lightweight neutral cables include the use of a force sensor at the end of the winding/unwinding unit. However, these solutions are expensive, and the instrumented winch system must be carefully designed. In addition, the longer the cable, the more difficult it will be for these solutions to acquire information about the cable tension state on the ROV side.

The contributions of this work include the following:

- The modeling, design, and implementation of the compliant-actuated system to equip the tether, which is composed of two symmetric buoys, one ballast, and one flex sensor located at the ballast;
- Tether length control by the feeder system on the surface, used to maintain the tether in a semi-stretched shape according to flex sensor feedback from the ROV;
- Simulations and real experiments to validate the solution by employing a compact underwater vehicle and a neutrally buoyant tether.

The paper is organized as follows. Section 2 focuses on the modeling of the buoy–ballast sensing system. Section 3 describes the simulations that were conducted to test the system. Section 4 details the system setup, sensor layout, control scheme, and experimental trajectories carried out in water pools. Section 5 is dedicated to the discussion of the results.

2. Modeling of The Compliant Buoy–Ballast Sensing System

2.1. Neutral Buoyancy of The Buoy–Ballast System

Given a neutrally buoyant tether, the static equilibrium of the buoy–ballast system, namely the V-system, depends on the apparent weights of the buoys and the ballast. The ballast is placed between the two identical buoys on the cable (Figure 1). In order to

ensure a neutral balance, the apparent weight of the ballast must be compensated by the apparent weights of the buoys:

$$W_{buoy} = |\rho_{buoy} - \rho_w|.V_{buoy}.g = (\rho_w - \rho_{buoy}).V_{buoy}.g \quad (1)$$

$$W_{ballast} = (\rho_{ballast} - \rho_w).V_{ballast}.g = 2.W_{buoy} \quad (2)$$

where W_{buoy} and $W_{ballast}$ stand for the gravity forces minus the buoyancy of the buoy and ballast, respectively. ρ_{buoy}, $\rho_{ballast}$, and ρ_w are the density of the buoy, ballast, and water, respectively. V_{buoy} and $V_{ballast}$ designate the volumes of the buoy and the ballast, respectively. g is the gravity constant.

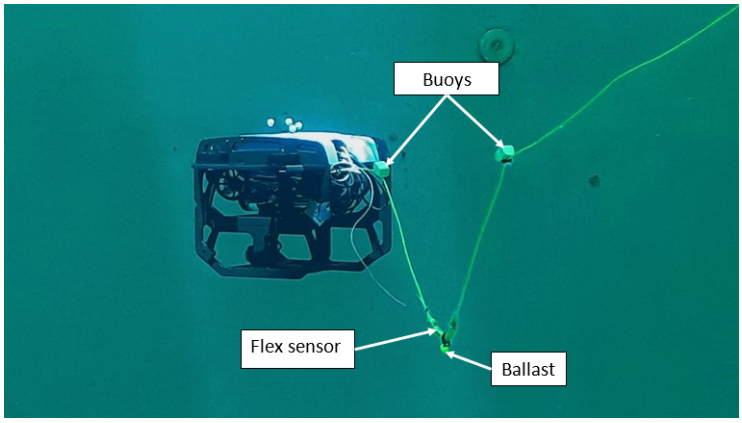

Figure 1. The compliant buoy–ballast system mounted on a neutrally buoyant cable.

The ballast is chosen from among off-the-shelf spherical weights, and the volume of the buoy is adjusted by machining it into a cuboid shape with rounded edges, since it is made of foam (LAST-A-FOAM®R-3318), taking into account the following equation obtained from the above equations:

$$V_{buoy} = \frac{1}{2}.\frac{\rho_{ballast} - \rho_w}{\rho_w - \rho_{buoy}}.V_{ballast} \quad (3)$$

2.2. Drag Forces

In steady state, the velocities of the buoys and ballast are considered constant, and a static analysis is conducted to estimate the relationship of the distance between the buoys as a function of the drive speed. The forces exerted by the fluid on the buoys and the ballast depend on the type of flow, which can be laminar, turbulent, or in a transitional state between both.

Usually, the moving object's related Reynolds number is used to identify the type of water flow around the object, regardless of whether it creates turbulence:

$$Re = \frac{\rho_w.v.L}{\mu} \quad (4)$$

where v is the relative speed between the object and the fluid, μ is the water viscosity, which is approx. 10^{-3} kg/m/s at 20 °C, and L is the characteristic length of the object, perpendicular to the direction of motion, such as for the diameter of a sphere. For a Reynolds number below 10, the flow can be considered as laminar, which is the case for very small objects. Above 10^6, the flow is turbulent at the surface and behind the object. Between 10 and 10^6, the flow can be either laminar or turbulent, or in a transitional state.

The order of magnitude of a 4 cm long compact buoy or ballast, moving at the average speed of 0.5 m/s is

$$Re = \frac{10^3\ 0.5\ 4.10^{-2}}{10^{-3}} \approx 2.10^4 \quad (5)$$

When the water flow is laminar, the drag force F_d^{lam} is proportional to the velocity, where the drag force in turbulent flow is quadratic, namely F_d^{turb}. The formulae for these two forces are given below.

$$F_d^{lam} = k.\mu.v \quad (6)$$

$$F_d^{turb} = \frac{1}{2}.C_D.A.\rho_w.v^2 \quad (7)$$

where

- k is a coefficient that depends on the shape of the object. For a sphere of radius R, $k = 6\pi.R$.
- C_D is the dimensionless quadratic drag coefficient, which is a property of the object. For a spherical shape, $C_D^{ballast} \approx 0.47$, and for a cuboid shape, $C_D^{buoy} \approx 1.05$.
- A is the cross-sectional area of the object, perpendicularly to the motion, which can be approximated by $\pi.R^2/2$, with $R = L/2$.

2.3. Distance Versus Speed in Steady-State Mode

Figure 2 presents the scheme of the buoy–ballast V-shape model, showing the forces exerted on the buoys and ballast. It is assumed that the entire system moves at a constant velocity v driven by the ROV in the left–right direction.

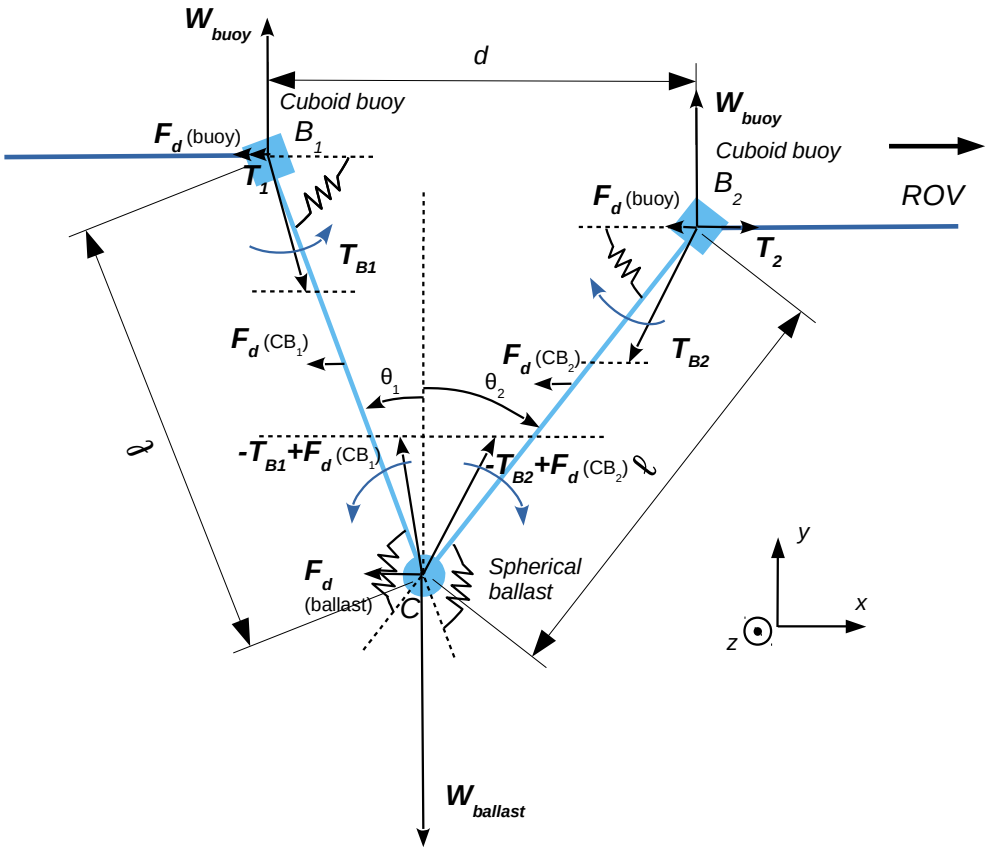

Figure 2. Model of the buoy–ballast V-system. The buoys and ballast move at the same constant speed.

The total number of independent equations that govern the force compensation of the elements of the V-shape system at constant speed is 7 (detailed in Appendix A), which are

$$T_{B1}^{x} = F_d^{buoy} + T_1 \quad (8)$$

$$T_{B1}^{y} = -W_{buoy} \quad (9)$$

$$T_{B2}^{x} = -F_d^{ballast} - F_d^{CB_1} - F_d^{CB_2} - F_d^{buoy} - T_1 \quad (10)$$

$$T_{B2}^{y} = -W_{buoy} \quad (11)$$

$$T_2 = 2.F_d^{buoy} + F_d^{ballast} + F_d^{CB_1} + F_d^{CB_2} + T_1 \quad (12)$$

$$(F_d^{buoy} + T_1 + \frac{1}{2}.F_d^{CB_1}).\ell.\cos\theta_1 - W_{buoy}.\ell.\sin\theta_1 = -C_s\left[2(\frac{\pi}{2} - \theta_1) + (\frac{\pi}{2} + \theta_2)\right] \quad (13)$$

$$-(F_d^{ballast} + F_d^{buoy} + T_1 + F_d^{CB_1} + \frac{1}{2}.F_d^{CB_2}).\ell.\cos\theta_2 - W_{buoy}.\ell.\sin\theta_2 = C_s\left[2(\frac{\pi}{2} + \theta_2) + (\frac{\pi}{2} - \theta_1)\right] \quad (14)$$

where

- T_{B1}^{x} and T_{B1}^{y} are the components of the force $\mathbf{T_{B1}}$ that is exerted by the cable portion CB_1 of length ℓ onto the left buoy.
- T_{B2}^{x} and T_{B2}^{y} are the components of the force $\mathbf{T_{B2}}$ that is exerted by the cable portion CB_1 of length ℓ onto the right buoy.
- F_d^{buoy} is the intensity of the drag force exerted by the fluid on the buoy.
- $F_d^{ballast}$ is the intensity of the drag force exerted by the fluid on the ballast.
- $F_d^{CB_1}$ and $F_d^{CB_2}$ are, respectively, the intensity of the drag force exerted by the fluid on the cable portion CB_1 and CB_2.
- C_s is the bending stiffness coefficient of the cable.
- θ_1 and θ_2 are, resp., the vertical angle of the CB_1 cable portion and the CB_2 cable portion.
- T_1 is the magnitude of the horizontal scalar force exerted by the cable that links the left buoy to the remote station.
- T_2 is the horizontal scalar force exerted by the cable that links the right buoy to the ROV. In the case of the figure, the intensity T_2 is positive since the ROV pulls on the cable to move from left to right.

The drag force magnitudes $F_d^{CB_1}$ and $F_d^{CB_2}$ are calculated as follows, based on the diameter d_c of the cable

$$F_d^{CB_1} = \frac{1}{2}.C_D^{cable}.d_c.\ell.\cos\theta_1.\rho_w.v^2$$

$$F_d^{CB_2} = \frac{1}{2}.C_D^{cable}.d_c.\ell.\cos\theta_2.\rho_w.v^2$$

where C_D^{cable} is dependent on the ratio of length to diameter.

The forces exerted on the portion of cable from the station to B_1 are the drag force, namely T_1^d, and the resisting force exerted by the winch on the station side, namely T_{1c}, which depends on the design of the feeder rotary joint. Since the cable is neutrally buoyant, there is no horizontal tension caused by apparent gravity (which would exist in the case of a weighing cable that takes the shape of a catenary in resting mode).

$$T_1 = T_1^d + T_{1c}$$

where T_1c is considered as a constant in the steady-state mode, whereas T_1^d can be expressed as

$$T_1^d = \frac{1}{2}C_D^{cable}.d_c.dh.\rho_w.v^2$$

where dh is the depth offset between B_1 and the other extremity of the cable on the station side.

Equations (13) and (14) can be numerically solved for θ_1 and θ_2 to obtain the evolution of the inter-buoy distance $d = \ell(\sin\theta_1 - \sin\theta_2)$ as a function of the velocity v (see Section 3.3).

After linearization using small angles, the horizontal distance d between the buoys can be calculated as

$$d \approx \ell(\theta_1 - \theta_2) \tag{15}$$

$$\approx \ell.\frac{\ell(F_d^{ballast} + 2.F_d^{buoy} + 2.T_1 + \frac{3}{2}F_d^{CB_1*} + \frac{1}{2}F_d^{CB_2*}) + 3\pi.C_s}{\ell.W_{buoy} + 3.C_s} \tag{16}$$

with $F_d^{CB_1*} = \frac{1}{2}.C_D^{cable}.d_c.\ell.\rho_w.v^2$ and $F_d^{CB_2*} = \frac{1}{2}.C_D^{cable}.d_c.\ell.\rho_w.v^2$.

The distance between buoys in the rest position can be calculated by zeroing the drag forces:

$$d_{rest} \approx \ell.\frac{2.\ell.T_{1c} + 3\pi.C_s}{\ell.W_{buoy} + 3.C_s} \tag{17}$$

Given the C_s value of cable stiffness and the estimation of T_{1c}, ℓ and V_{buoy} can then be adjusted to obtain the desired distance between buoys in the rest position.

2.4. Dynamics Analysis Through Differential Equations

Taking into account small angles, i.e., $\tan\theta_i \approx \sin\theta_i \approx \theta_i$, the dynamics equations of motion of the buoys in the left–right horizontal direction are

$$m_{buoy}\frac{dv_{B1}}{dt} = -F_d^{buoy,1} - T_1 + W_{buoy}.\theta_1 - \frac{C_s}{\ell}\left[2(\frac{\pi}{2} - \theta_1) + (\frac{\pi}{2} + \theta_2)\right] \tag{18}$$

$$m_{buoy}\frac{dv_{B2}}{dt} = -F_d^{buoy,2} + T_2 + W_{buoy}.\theta_2 + \frac{C_s}{\ell}\left[2(\frac{\pi}{2} + \theta_2) + (\frac{\pi}{2} - \theta_1)\right] \tag{19}$$

Then, distance d is expressed as

$$\frac{d(d)}{dt} = \frac{d(r_{B_1B_2})}{dt} = v_{B2} - v_{B1} \tag{20}$$

The subtraction of Equation (19) from (18) yields

$$m_{buoy}\frac{d^2(d)}{dt^2} = F_d^{buoy\,1} - F_d^{buoy,2} + W_{buoy}(\theta_2 - \theta_1) + T_{12} + 3.\frac{C_s}{\ell}(\theta_2 - \theta_1 + \pi) \tag{21}$$

with $T_{12} = T_1 + T_2$. Since $d \approx \ell(\theta_1 - \theta_2)$,

$$m_{buoy}\frac{d^2(d)}{dt^2} = F_d^{buoy,1} - F_d^{buoy,2} - \left(W_{buoy} + 3\frac{C_s}{\ell}\right).\frac{d}{\ell} + T_{12} + 3\pi.\frac{C_s}{\ell} \tag{22}$$

In addition,

$$F_d^{buoy,1} - F_d^{buoy,2} = D.(v_{B1} - v_{B2}) = -D.\frac{d(d)}{dt} \tag{23}$$

where

- $D = k.\mu$ for a laminar water flow.
- $D = D(v_{B1}, v_{b2}) = \frac{1}{2}.C_D.A.\rho_w.(v_{B1} + v_{B2})$ for a turbulent water flow.

Noting that $E = W_{buoy} + 3\frac{C_s}{\ell}$, the differential equation relative to d is the

$$m_{buoy}\frac{d^2(d)}{dt^2} + D.\frac{d(d)}{dt} + \frac{E}{\ell}.d \quad = \quad T_{12} + 3\pi.\frac{C_s}{\ell} \tag{24}$$

The undamped pulsation is $\omega_0 = \sqrt{\frac{E}{\ell.m_{buoy}}}$. The following transfer function of the linearized system can be written as

$$H(j\omega) \quad = \quad \frac{d}{T_{12} + 3\pi.\frac{C_s}{\ell}} = \frac{\ell/E}{1 + (j\omega)\frac{D.\ell}{E} + (j\omega)^2.\frac{\ell.m_{buoy}}{E}} \tag{25}$$

In the case of a laminar flow, the buoy–ballast system can be seen as a second-order low-pass filter for small angles with the damping coefficient $\xi = \frac{1}{2}.k.\mu.\sqrt{\frac{\ell.}{E.m_{buoy}}}$.
In the case of a turbulent flow, if we consider the sum of velocities $(v_{B1} + v_{B2})$ to be above a certain threshold and to vary around an average velocity v_s, then the buoy–ballast system can be seen as a second-order low-pass filter for small angles, with the damping coefficient $\xi = \frac{1}{2}.\frac{1}{2}.C_D.A.\rho_w.v_s.\sqrt{\frac{\ell.}{E.m_{buoy}}}$. The setting of the damping coefficient to a few units above 1, namely $\xi_{threshold}$, helps with adjusting parameters ℓ and V_{buoy} in minimizing v_s as much as possible, taking into account the other constraints (value of d_{rest} and ℓ not too high with regard to the size of the ROV):

$$\xi \quad > \quad \xi_{threshold} \tag{26}$$

$$v_s \quad > \quad \frac{4}{C_D.A.\rho_w}.\sqrt{\frac{E.m_{buoy}}{\ell}}.\,\xi_{threshold} \tag{27}$$

2.5. Conclusions on the Use of Modeling

The steady-state model is useful for determining the theoretical variation in the distance between the buoys as a function of the speed via numerical resolution. This theoretical variation is compared with the variation obtained in the simulator (see Section 3, dedicated to simulations, where the influence of T_{1c} is discussed). The steady-state model is also used in the control scheme to determine the target distance between buoys as a function of the ROV speed such that the whole system converges to the steady-state mode (see Section 4.2).

The dynamics analysis allows the behavior of the V-shape system to be determined as a second-order low-pass filter after linearization. However, as the system is underactuated, it is not possible to separately control the velocities of each of the buoys.

In addition, Equations (17) and (27) are used to define a zone of validity for parameters ℓ and V_{buoy}. The limits of the validity zone can be defined by the following equations:

$$d_{min} < d_{rest} < d_{max} \tag{28}$$

$$\frac{4}{C_D.A.\rho_w}.\sqrt{\frac{E.m_{buoy}}{\ell}}.\,\xi_{threshold} < v_s \tag{29}$$

using $d_{min} = 0.1m$, $d_{max} = 0.3m$, $\xi_{threshold} = 1$, and $v_s = 0.1\ m/s$, where these values are the result of design choices.

3. Simulations

This section focuses on the following:

- The numerical modeling of the V-shape system with Matlab–Simulink™ for precise sizing of the parameters ℓ and V_{buoy}.
- A series of simulations run with the Vortex® simulator to check the validity of the V-shape system. In particular, the variation in the distance between buoys as a function of speed is observed and compared with the variation obtained using the theoretical model to check the steady-state mode. The influence of the V-shape system in terms of

power consumption of the ROV is also evaluated. Then, a complete trajectory with varying depth, turns, and speed is simulated to observe the behavior of the V-shape system.

3.1. Numerical Modeling for Precise Sizing

For precise sizing purposes, the V-shape system was modeled using finite solids and simulated in the Matlab–Simulink environment using the Simscape and Multibody toolbox. This numerical model is composed of twenty-four 5 cm long rigid elements linked to their neighbors by revolute joints whose stiffness is equal to 10^{-3} N.m/rad, which was experimentally determined using the Fathom Slim tether cable of BlueRobotics™ [6]. The damping behavior is a result of the buoys' drag force. Figure 3 is a representative screenshot from the video that shows the dynamic behavior of the V-shape system returning to rest state. This validates the physical assumptions for the design of the proposed mechanical model. Moreover, it confirms that the V-shape system does not acquire a droplet shape, which is crucial for guaranteeing the monotony of the output signal provided by the flex sensor mounted at the ballast [27]. This embedded instrumentation provides a suitable signal related to the compliance state that is appropriate for use as feedback for the winch command.

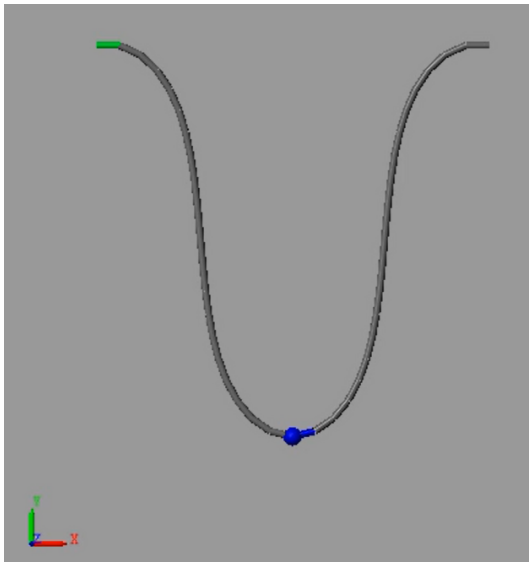

Figure 3. Snapshot of the numerical model obtained for the buoy–ballast system using Matlab–Simulink™ (https://www.youtube.com/watch?v=PtQigrKUr9E (accessed on 1st Dec. 2023).

The V-shape system should not be excessive in size with respect to the robot's dimensions. A distance of 1.2 m between the buoys was chosen for a 1 m range of distance compliance between buoys and a minimal distance of 0.2 m at rest, which yields ℓ = 0.6 m for each section CB_1 and CB_2. The value of V_{buoy} was set to approx. 36 cm^3.

3.2. Configuration for The Simulator

Simulations of the complete system, including the cable, buoy–ballast system, ROV (which is speed-controlled in open-loop), and cable feeder, were carried out using the Vortex® simulator, version 2021a (2021.1.0.66). This software integrates the modeling of cables from a mass–spring model, taking into account their physical parameters for realistic rendering. The tether is a complex non-homogeneous object comprising several twisted strands and different coating layers. Some of its physical parameters are assumed to be constant and are directly provided by the manufacturers or easy to measure directly through experimental setups. Other parameters are more difficult to determine, requiring the use of abacuses. Table 1 summarizes the parameters used for simulation. The simulated tether mimics the Fathom Slim tether. Breaking strength, radius, and linear density were

obtained from datasheets. Bending stiffness, torsional stiffness, axial stiffness, damping, and drag coefficients were determined through experiments [6].

Table 1. Parameters used for simulation of the Fathom Slim tether. Values marked with an asterisk (*) are approximate estimates.

Physical Parameters	Fathom Slim Tether	Unit
Axial stiffness	1.10^{12} *	N
Axial damping	$8,2.10^{14}$ *	kg.m/s
Bending stiffness	$5,7.10^{-4}$	$N.m^2/rad$
Bending damping	$2,9.10^{-4}$ *	$N.m^2/rad$
Torsion stiffness	$8,8.10^{-4}$	$N.m^2/rad$
Torsion damping	$8,8.10^{-5}$ *	$N.m^2/rad$
Linear density	2.10^{-3}	kg/m
Drag coefficient	1,8 *	-
Radius	2.10^{-3}	m
Breaking strength	1520	N

The simulated ROV is adapted from the BlueROV2-Heavy from BlueRobotics^{TM}, which has four vertical thrusters and four thrusters for the horizontal movements arranged in vectorial mode.

3.3. Study of The Distance Between Buoys

The distance between both buoys and its variation are observed while the ROV moves forward at a constant speed (Figure 4). The coordinates of the centers of the buoys are used to calculate the distance and the variation. In this simulation, the ROV starts at a horizontal distance of 4 m from the remote station and a depth of 0.5 m. A length of 10 m of cable is unwound and then, at 11 s, the ROV starts to move 7 s forward at a controlled speed of 0.4 m/s. The desired speed is reached after 1.3 s. During the simulation, the difference between the length of the deployed cable and the distance of the ROV from the remote station is greater than 3 m. The time evolution of the distance between buoys shows that the system returns to its rest position in 5.5 s after the ROV stops. The 5% response time is 3.8 s. Thus, the system behaves like a damper. The impact of the 120 ms delay of the flex sensor, due to filtering post-processing, is negligible, and the acquisition/control frequency of 25 Hz is sufficient. Despite the damping effect, the variations in ROV speed immediately affect the distance between the buoys, which supports the interest in using this parameter to control the automatic distribution of the cable.

To observe the behavior of the damped system, the relationship between the distance between the buoys and the ROV forward speed at 0.5 m depth is shown in Figure 5. The figure displays the curve obtained from simulation and the curves obtained from the theoretical model for values of T_{1c} equal to 0 N , 0.01 N, 0.03 N, 0.05 N, and 0.1 N. The drag forces were considered quadratic. Despite some slight offset, the curve issued from the steady-state model with an order of magnitude of 0.03 N for T_{1c} is close to the curve obtained in the simulation. The value of T_{1c} depends on the design of the feeder built for the simulation. The inter-buoy distance is close to its maximum when the ROV reaches a speed of 0.8 m/s. This value represents the speed limit for optimal behavior of the system. The distance versus speed relationship can be used to define a target inter-buoy distance as a function of the ROV speed to help the system converge to the steady-state mode. this is not possible since labels are not compatible with tex symbols

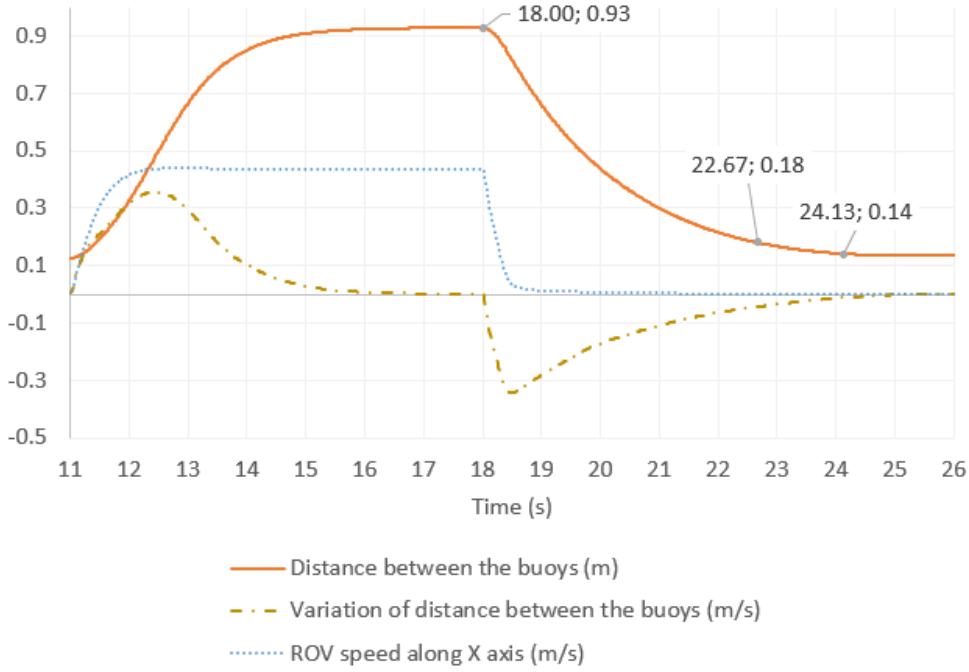

Figure 4. Distance between buoys and its variation when the ROV moves at constant speed.

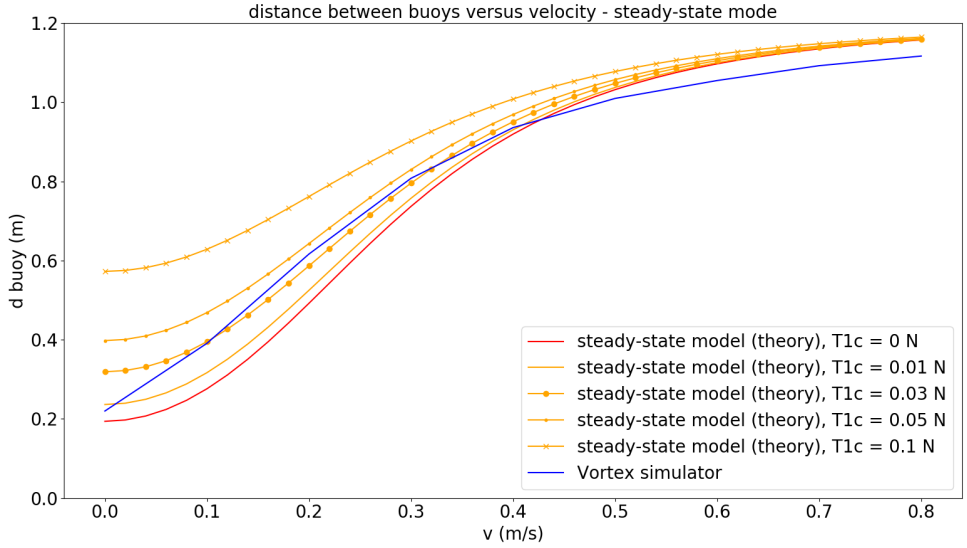

Figure 5. Distance between buoys versus ROV speed. Comparison between theoretical steady-state model and simulation using Vortex. Influence of T_{1c}, the constant part of the cable tension from the left side.

3.4. Influence of Buoy–Ballast System on ROV Power

The power of the ROV is calculated using the manufacturer data of the T200 brushless motors that equip the BlueRov. The manufacturer datasheets provide the motor power as a function of the motor speed, and the thrust as a function of the motor speed. The motors' speeds are controlled to achieve the desired vehicle speed. The total power is then calculated by summing the motor powers.

The speed of the ROV is not affected by the presence of the compliant system since the simulated ROV is velocity-controlled. However, the total power of the ROV thrusters observed in simulation, represented in Figure 6, is 2% higher globally with the compliant system. This is due to the drag forces on the buoy–ballast system that the cable transmits

to the ROV. The passive compliant system introduces slightly more tension in the cable throughout the movement of the ROV compared with a free cable with sufficient length. However, this increase in tension is not significant, and the compliant system on the cable prevents the cable from pulling strongly on the ROV.

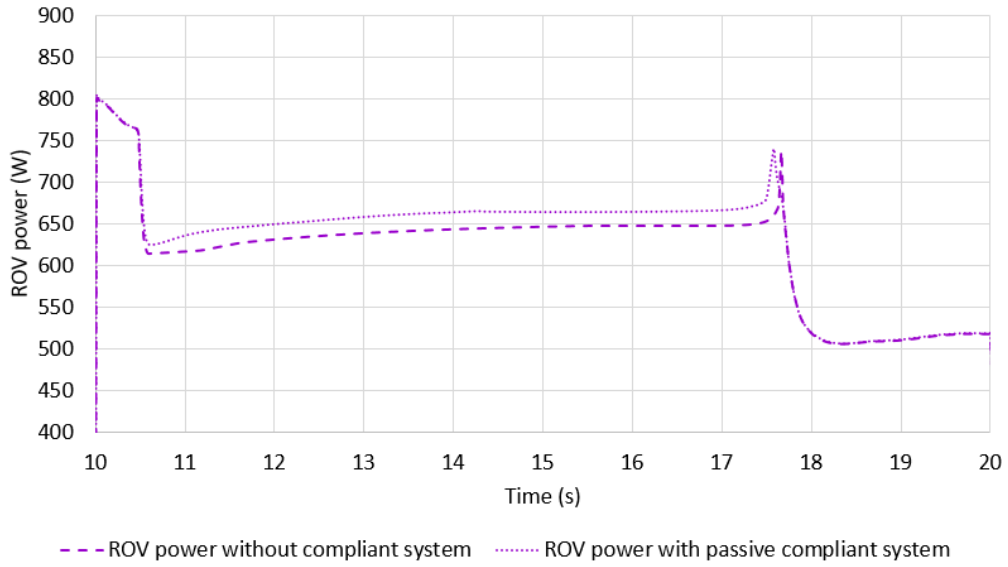

Figure 6. Comparison of cable impact on ROV power with and without passive compliant system.

3.5. Generation of ROV Trajectories for Further Analysis

Generation of trajectories. Trajectories are defined as a sequence of depth, orientation, and speed commands of the ROV. The ROV is speed-controlled with a PID control loop and with a proportional control loop in heave, yaw, roll, and pitch. Figure 7 presents the curves for the velocity, depth, and angle commands as well as the values measured during the simulation for an untethered ROV. Keyframes are indicated on this trajectory to provide reference points. This trajectory starts with forward movement of the ROV along its longitudinal axis at different successive speeds between points 0 and 1 (0.1 m/s, 0.2 m/s, and then 0.3 m/s) in parallel with a depth control of 0.5 m. Then, a command for a forward speed of 0.3 m/s is sent again (point 1), followed by a depth command at 2 m (point 2). Then, while moving forward at a constant speed, the ROV receives successive yaw commands: 45 deg to the left (point 3), 45 deg to the right (point 4), 0 deg, 90 deg to the right (point 5), and 180 deg (point 6). Finally, the forward speed command is set to zero, while the depth command is kept to 2 m (point 7). The trajectory projected in the horizontal plane, deduced from the longitudinal speed and the orientation of the ROV, is also presented at the bottom right. The difference between the set point and the actual displacements of the ROV is due to hydrodynamic phenomena, which slow down the ROV in water. Moreover, when there are changes of set point in depth and yaw, a significant acceleration is required, resulting in overloading of the thrusters and affecting the speed along the x-axis (Figure 7).

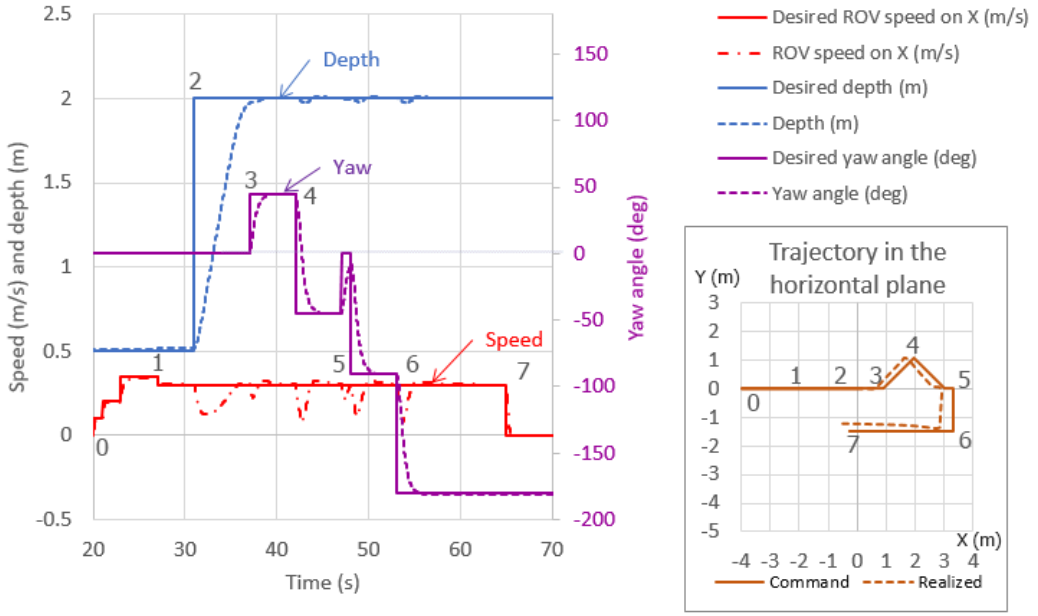

Figure 7. Simulated trajectories of the ROV.

Control schemes. The behavior of the system is compared for five different modes listed below.

- Cable not controlled and without compliant system: the cable length is fixed to 15 m along the simulation.
- Cable with passive compliant system (not controlled): the cable length is fixed to 15 m along the simulation.
- Cable controlled with ROV speed command as input: the delivery speed of the cable is set to the ROV speed.
- Cable controlled with distance between the buoys: a closed-loop PD controller maintains a target distance of 0.8 m between the buoys.
- Hybrid control of the cable based on ROV speed and distance between buoys, which combines buoy distance PD controller and P controller using an ROV speed command. Furthermore, the target distance between the buoys is set to vary according to the ROV speed. The proportional part of the PD controller on the buoys' distance works only if the distance is at least 5 cm longer than the target (taut cable) or if it is less than the target for more than 1 s (slack cable).

Distance between buoys. Figure 8 depicts the evolution of the distance between buoys for passive configuration and the three control modes.

Unsurprisingly, the best control is obtained with the buoy distance-based control, which keeps the distance between buoys around 0.8 m, despite oscillations that appear when the ROV is turning, from keyframe 3 to shortly after keyframe 6. The hybrid controller allows the distance to be kept within reasonable values, between 0.4 m and 0.9 m. The distance between the buoys reaches more extreme limits (0.16 m and 1.1 m) when the cable is not controlled or ROV speed-controlled.

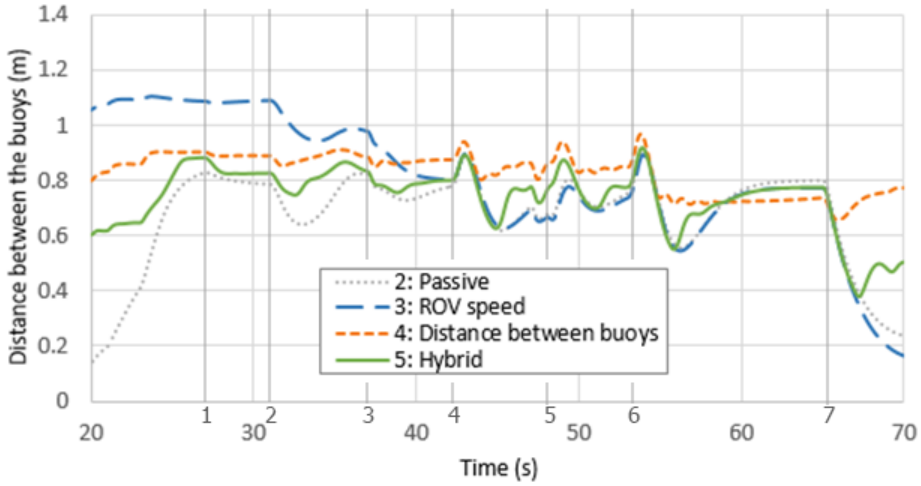

Figure 8. Comparison of the evolution of the distance between the buoys in passive mode and in three control modes.

Cable delivery speed. Figure 9 shows the delivery speed for the three control modes.

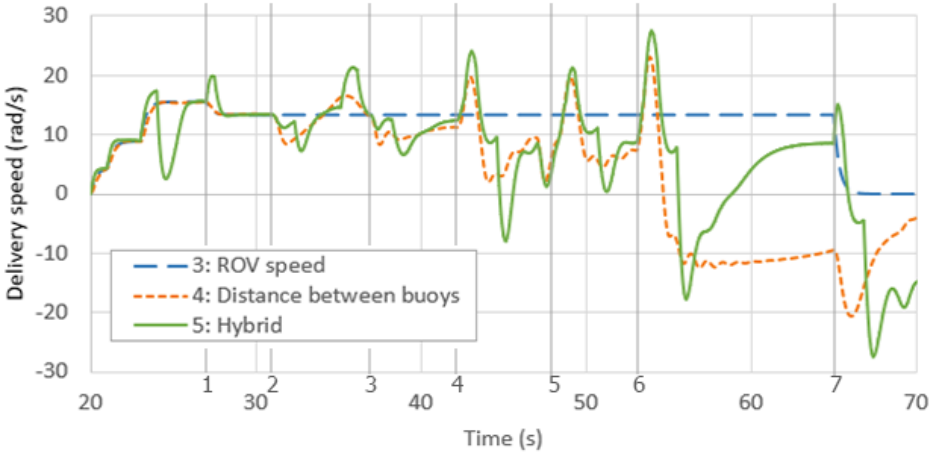

Figure 9. Comparison of the delivery speed for different control modes with a complex trajectory.

When the ROV moves forward at low speed (before keyframe 1), the feeder's speed is almost the same for the three control modes. As only the linear speed is considered for the ROV speed-based control, the cable delivery speed remains constant between keyframes 1 and 7, not taking into account the orientation of the ROV. Oscillations are more pronounced for the hybrid controller than for the buoy distance-based controller, resulting in a smoother cable delivery speed.

Overall cable shape. The overall shape of the cable is depicted in Figure 10 for all cable control configurations at two different keyframes of the trajectory, namely keyframe 5, when the ROV finishes its forward motion, and after keyframe 7, when the ROV returns close to the feeder. With the hybrid control, the cable behaves correctly, except for when a slight excess of cable forms a lobe as the ROV moves toward the feeder. The length of free cable is too long with the ROV speed controller. In contrast, the length of free cable is tightly adjusted when using the buoy distance-based controller. When the cable is not controlled, loops appear on the water surface before the ROV starts to move away, as the cable length is far too long. These loops remain throughout the trajectory, generating a significant risk of snagging or entanglement of the cable.

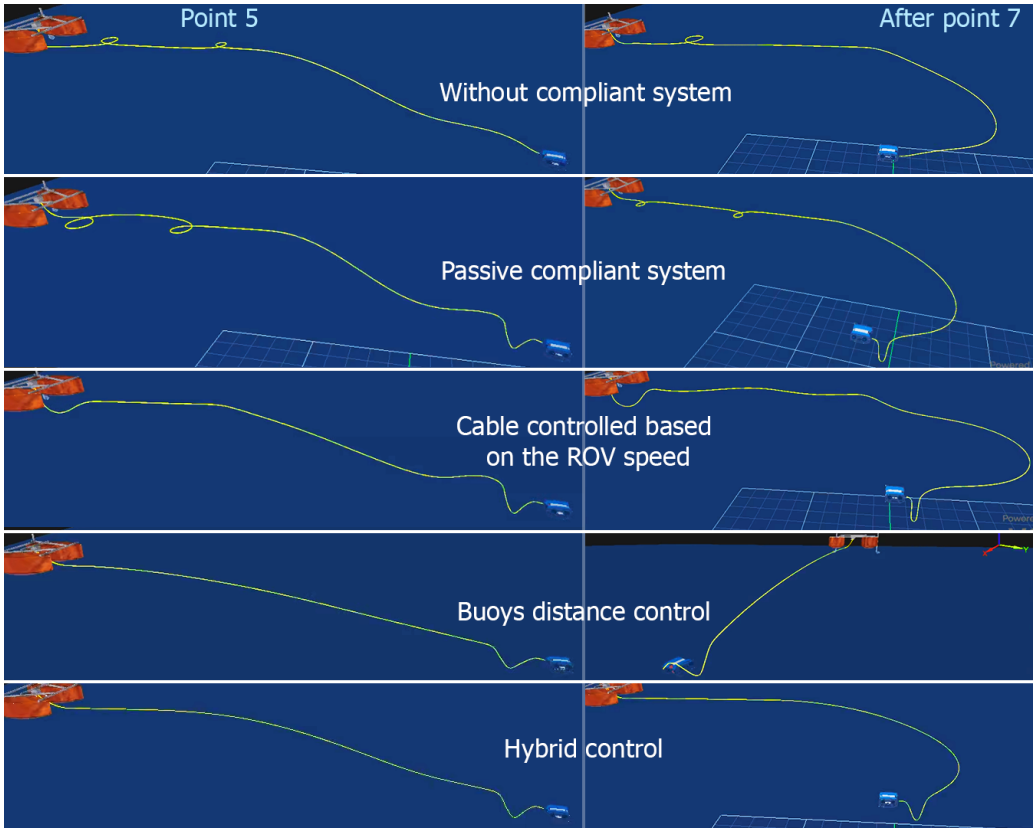

Figure 10. Views of the system configuration for di this is not possible since labels are not compatible with tex symbolsfferent cable control modes at two points of the complex trajectory (video available at this link: https://www.youtube.com/watch?v=ZC2zStwkdSo (accessed on 1st Dec. 2023)).

Conclusions from controller analysis.

- Of the three controllers evaluated in the simulation, the ROV speed-based controller is not sufficiently responsive and generates a static error on the buoys' distance that is never corrected. It is therefore not robust to external disturbances.
- The control mode based on the distance between buoys is rather smooth, robust, and reactive.
- The hybrid control is quite reactive but presents some more pronounced oscillations while remaining rather stable. Hybrid control could possibly be improved by replacing the ROV command speed with the actual ROV speed, which would require the use of more sensors on the ROV, such as a Doppler velocity log (DVL).

4. Description of Setup, Control Mode, and ROV Trajectories for Real Experiments

The simulations described in the previous section allowed validation of the behavior of the V-shape system by comparing the different modes of cable control. This section describes the preparation for real experiments that took place in water tanks. This preparation includes the setup, control scheme, and two kinds of trajectories that were used to check the system behavior in real conditions. To ensure the ground truth of the movements of the cable, compliant buoy–ballast system, and ROV, an underwater motion capture system was implemented.

4.1. Setup

The cable feeder was fixed on the border of a 16 × 8 m water tank and connected to the ROV through a 25 m long 4 mm diameter tether, namely the Fathom Slim, equipped with the buoy–ballast system, of which a technological description can be found in [27]. The ROV used was a BlueROV2-Heavy, as in the simulation.

A flex sensor was mounted on the cable at the ballast location using a fixed bracket and guides along the cable (Figure 11). The sensor has negligible bending stiffness. It was wrapped in a thin plastic envelope for waterproofing. The sensor resistance varies when the cable is bent. This varying resistance is transformed into a voltage signal through a voltage divider, then filtered, centered, and trimmed. The variation in the resulting signal is used to fit the corresponding distance between the buoys through a third-order polynomial (Figure 12).

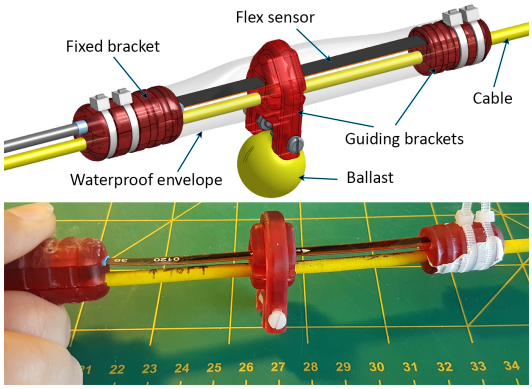

Figure 11. Mounting of the flex sensor near the eballast.

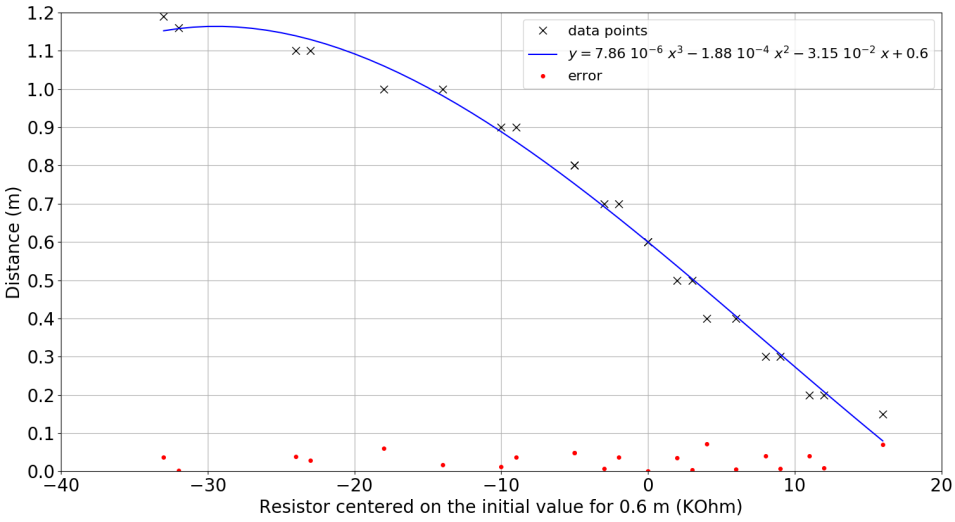

Figure 12. Measured distance between the buoys as a function of the centered resistance of the flex sensor with experimental data points.

Table 2 summarizes the characteristics of the buoy–ballast system to which the Fathom Slim tether is equipped, taking into account the previously described modeling analysis.

Table 2. Specifications and characteristics of the buoy–ballast system adapted for the Fathom Slim tether.

Overall buoyancy	Neutral
Distance between ballast and buoy	0.6 m
Buoy size	$29 \times 29 \times 47$ mm^3
Buoy foam density	288 kg/m^3
Ballast mass	76 g
Ballast diameter	25 mm
Flex sensor model	FS-L-0095-103-ST (Spectra Symbol)
Flex sensor size	110 mm long, 0.5 mm thick

The controller board inside the robot was run on a Linux/ROS-1 system with the *mavros* library to interface the high level control with the autopilot *ArduSub*. The BlueROV2 was controlled remotely via a gamepad connected to the control computer. The remote control computer contains the embedded ROS *master*. It was connected to the feeder for the transmitting of control commands while taking into consideration the data received from the flex sensor through the ROS system embedded in the robot. The diagram in Figure 13 shows the architecture of the ROS *nodes* for controlling the global system during the experiments.

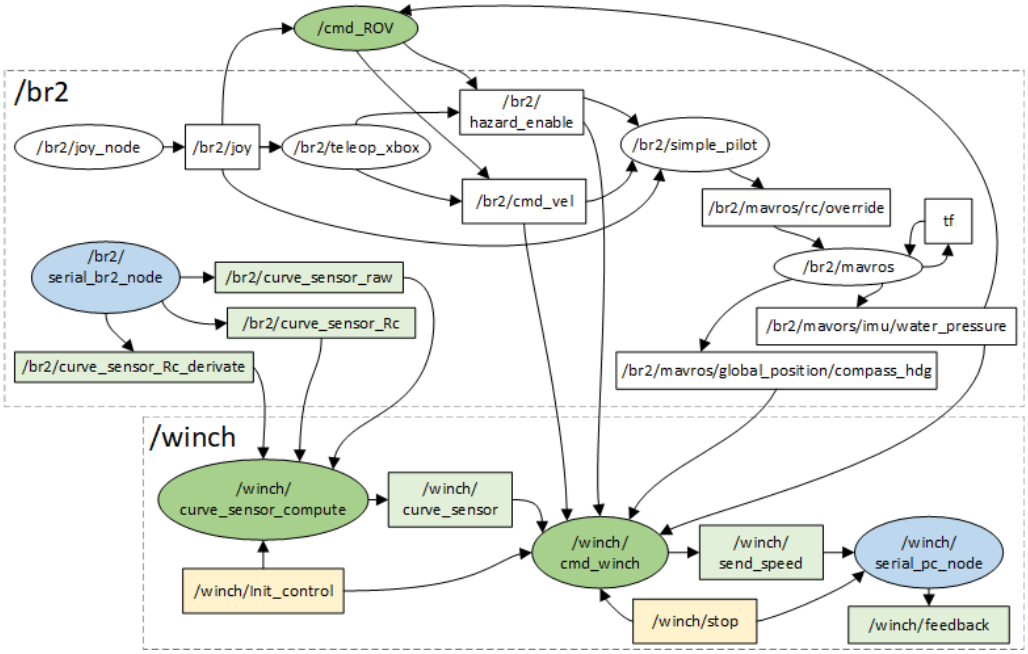

Figure 13. Graph of the global ROS nodes architecture for the control. The oval boxes correspond to the *nodes* and the rectangular boxes to the topics exchanged by these *nodes*.

The robot and the cable were tracked by a camera motion-tracking system, namely *Qualisys*, with five underwater optical cameras *Miqus M5u* at 180 frames per second. The cameras use blue LEDs, whose light is reflected by markers placed on the ROV and the cable. Data are recorded from the *QTM* software, version 2020.3 build 6020, which is controlled from a dedicated computer during the experiments. This software computes the current 3D position of each marker provided they are detected by several cameras. Across the experiments, the position residuals of the markers were about 1.3 mm for the ROV, with a minimum of 0.9 mm and a maximum of 10 mm.

4.2. Control Scheme

Figure 14 is the control block diagram of the feeder, which can be controlled using the measured distance between buoys, namely buoy gap on the figure, or using a desired cable length. The control for the feeder consists of a main control loop with proportional controllers, which includes a speed control loop with a proportional–integral controller and anti-windup system. Flex sensor processing, presented in Section 4.1, is used to estimate the inter-buoy distance, which is sent to the feeder by the ROV.

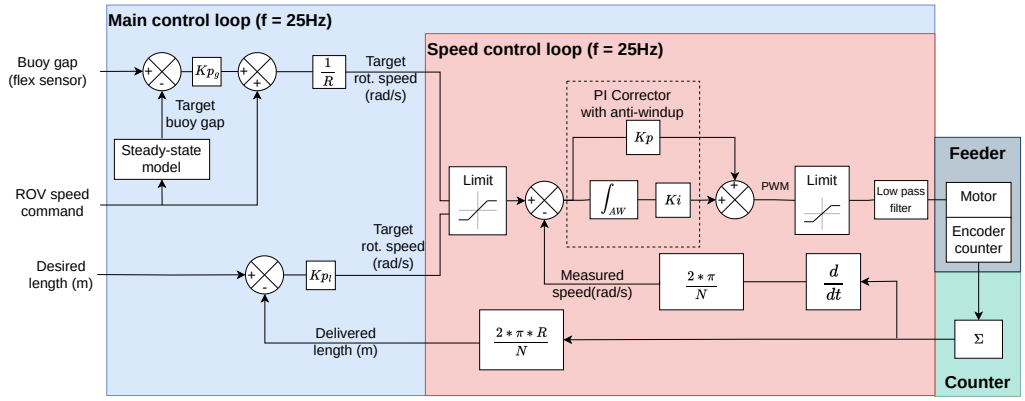

Figure 14. Control block diagram of the feeder using the steady-state model and length and speed control loops. R is the radius of the feeder wheel and N is the number of ticks of the encoder counter.

In normal mode, namely buoy gap control mode, the feeder speed is controlled as the ROV moves to regulate the gap between both buoys. The target buoy gap is defined from the actual ROV speed using the steady-state model that gives the variations in the buoy gap as a function of the ROV speed (see Section 2.3 and Figure 5). The target buoy gap is then compared to the current gap measured by the flex sensor to update the rotation speed of the feeder.

In length control mode, the cable length can be directly controlled by setting a desired length. The feeder can actually be operated to release the cable when necessary; e.g., when the V-system is stretched, 2 m of cable is uncoiled after a 10 s period until the V-system is released.

Buoy gap control and length control modes are separately activated as required. Cable length is computed in the speed control loop such that it is accessible even when length control is disabled. The target rotation speed is first bounded to avoid exceeding the motor limits. Embedded in the speed control loop is a proportional–integral corrector, which is applied to the error between the bounded target speed and the measured speed. This corrector has an anti-windup system that limits the sum of past errors to stabilize the system. It outputs a raw PWM signal, which is then bounded and smoothed by a low-pass filter before being transmitted to the motor control board.

4.3. Trajectories

The experimental results of cable control validation were obtained during a series of tests carried out in the pool of the CIRS (Underwater Robotics Research Center) in Girona in the context of a TNA (TransNational Access) European project.

Two kinds of ROV trajectories were defined to represent two configurations where cable control must be useful to reduce risks of cable snagging or entanglements as below.

- A linear trajectory where the ROV goes forwards and then backwards. First, a forward thrust command of 25% is sent for 15 s (between keyframes 1 and 2). Then, a zero command is sent for 5 s (between points 2 and 3). Finally, a backward thrust command of 25% is sent for 10 s (between points 3 and 4).
- A curvilinear S-shape trajectory comprising the following steps :
  - a forward thrust of 40% for 15 s (between points 1 and 2);

- a right turn composed of a yaw thrust of 11.25% combined with a forward thrust of 40% for 6.5 s to turn right (between points 2 and 3);
- a left turn with the same thrust command values as the left turn, for 6 s (between points 3 and 4);
- a forward thrust of 40% for 4 s (between points 4 and 5).

All these trajectories were associated with 1.5 m depth control. The ROV was open-loop-controlled to follow these trajectories by driving the corresponding thrusters.
For each trajectory, three kinds of cable management were tested:

- Passive slack cable, where cable of sufficient length was deployed in the water from the beginning.
- Passive taut cable, where the cable is stretched between the feeder and the ROV when the ROV moves away from the feeder, which means that the buoy–ballast system is also completely stretched and has no real influence on the ROV. The feeder is not powered. When the ROV comes closer to the feeder, the cable is no longer taut, and the buoy gap tends to be reduced to a minimum.
- Cable control, using buoy gap control mode. A 25% and 40% forward thrust is associated with a buoy gap of about 0.7 mn and 0.8 m, respectively, according to the steady-state model.

5. Results And Discussion

5.1. Linear Trajectory

Figure 15 illustrates the cable management results for the linear trajectory including buoy distance control mode, passive slack mode, and passive taut mode. The feeder appears to be quite reactive and smooth in winding/unwinding the cable depending on ROV motion and the distance between buoys. The buoy–ballast system exhibits highly dynamic transient behavior between points 2 and 4 due to the changes in velocity. When moving backward, the feeder also takes more time for buoy gap convergence back to the target distance (0.7 m).

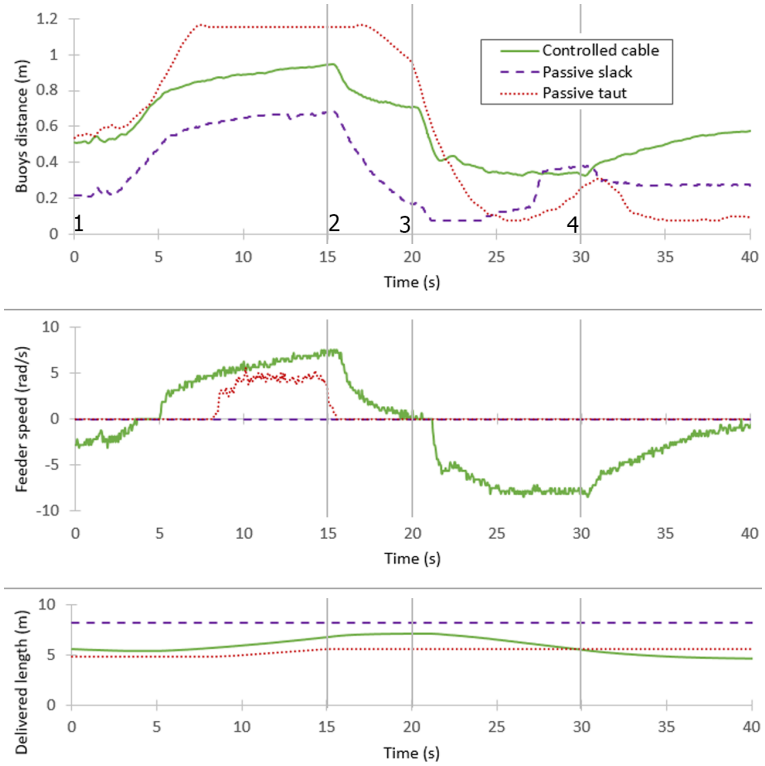

Figure 15. Distance between buoys, feeder speed, and unwound length of cable in control mode, passive slack mode, and passive taut mode for forward–backward trajectory. (https://youtu.be/owekUkN_UtMforcontrolmode, https://youtu.be/1RTT23-USDYforpassivetautmode, https://youtu.be/FG5iyNfjzckforpassiveslackmode (accessed on 1st Dec. 2023)).

Figure 16 presents the paths followed by the ROV projected onto the horizontal plane as measured by the *Qualisys* system for the three cable modes.

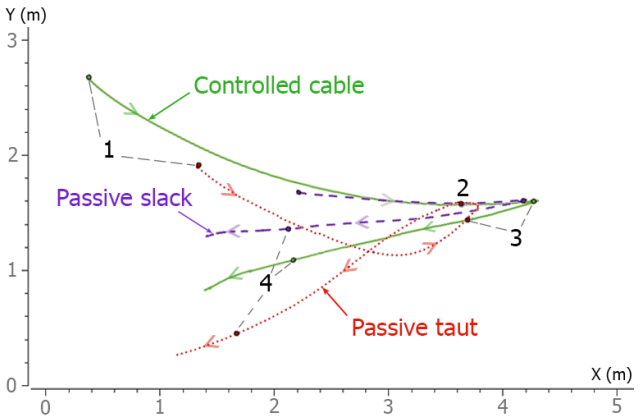

Figure 16. Top view of actual forward–backward trajectories of the ROV using cable control, slack, or passive taut cable. Paths are superimposed at point 2 for easier comparison.

If there were no external disturbances at all, the path would be rectilinear. The ROV shifts slightly to the left when the cable is slack. This deviation is slightly larger in the control mode and is observed during both its forward and backward motion. The deviation is significantly greater in passive taut mode. Furthermore, the distance covered by the ROV is shorter with the taut cable.

Figure 17 shows the evolution of depth control of the ROV for the three modes. Only the control mode is efficient in helping to regulate the ROV depth. In addition, the vertical

thrusters' work significantly increases more when the cable is not controlled than when it is controlled.

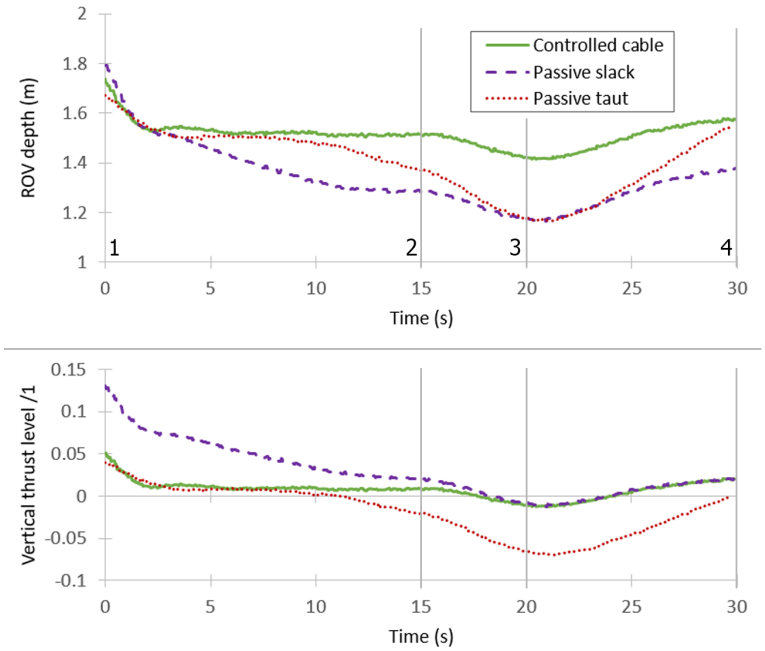

Figure 17. ROV depth and vertical depth control thrust in the three modes.

5.2. Curvilinear Trajectory

Figure 18 shows the snapshots at keyframes 1, 3, and 4 in cable control mode. Figure 19 presents the results in terms of buoy gap, feeder speed, and delivered cable length. Figure 20 presents the yaw angle. Figure 21 shows the executed trajectories in the cases of passive slack cable, passive taut cable, and control mode.

In control mode, the compliant system keeps its V-shape and a buoy gap average close to the target distance (0.8 m), except for during turns, where the behavior is highly dynamic because of the increased forward speed and the opposing directions of the successive turns, which causes the buoy gap to reach its bounds, namely 0.2 m and 1.2 m, during a short period of time. The buoy gap resulting from passive taut and passive slack modes demonstrates the added value of automatic cable length management in maintaining an average buoy gap, which allows the cable shape between the station and the buoy–ballast system to be controlled.

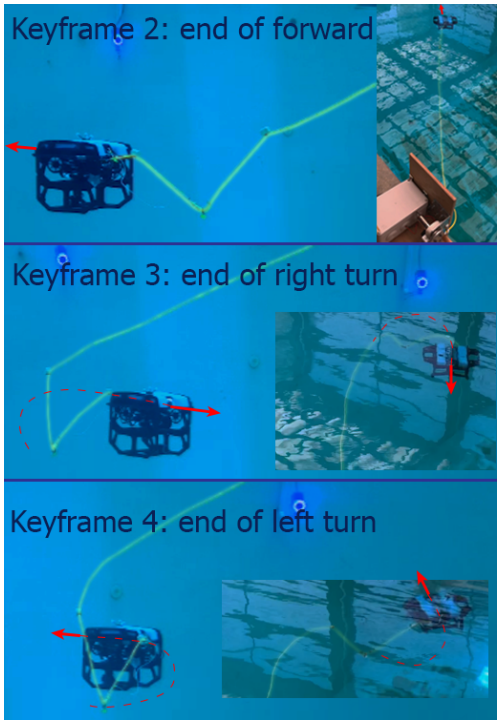

Figure 18. Views of the overall system at different points along the curvilinear trajectory when the cable is controlled. The red arrows indicate the direction of motion of the ROV (video at https://youtu.be/fy-JTc8PvIY (accessed on 1st Dec. 2023)).

For a flawless system without any disturbance, the yaw angle (Figure 20) must be constant during the ROV straight line commands (before point 2 and after point 5). It must also be linear during rotating commands (between points 2 and 3, then 3 and 4). There is a slight deviation of about 20 deg to the right during the first straight line (2.6 m) command of the ROV for the passive slack cable. This deviation is oriented to the left and its absolute value is doubled with the controlled cable and doubled again with the passive taut cable. In fact, the cable is fixed on the left side of the back of the ROV, which induces a slight deviation to the left for the controlled cable, both in a straight line and during a right rotation. This deviation is much larger for the passive taut cable. The left rotation of the ROV appears to be less affected in the control and passive taut modes.

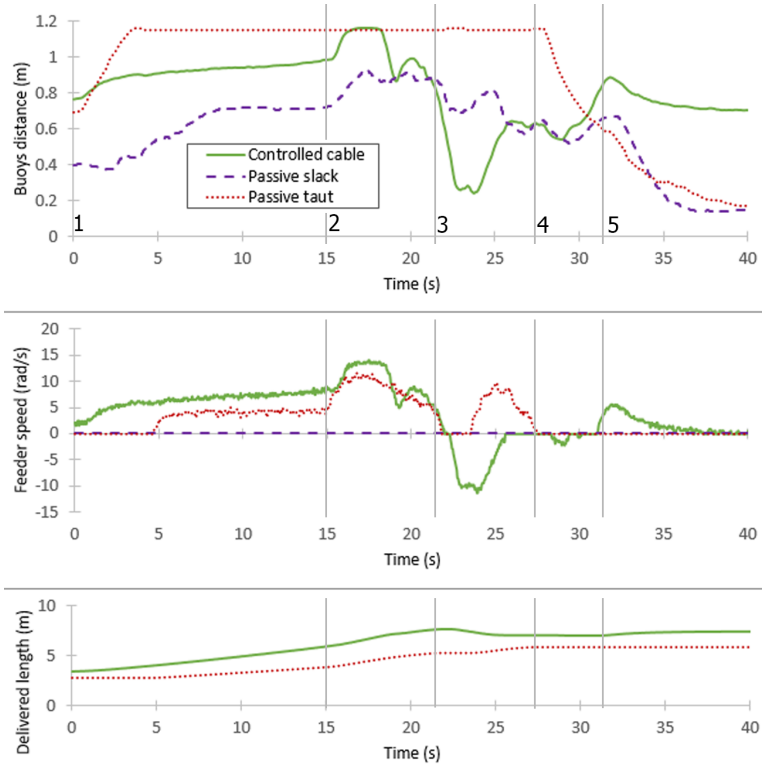

Figure 19. Distance between buoys (flex sensor), feeder speed, and unwound length of cable in control mode, passive slack mode, and passive taut mode for the curvilinear trajectory (videos at https://youtu.be/LR4BKefRSnM for passive slack mode and at https://youtu.be/74p5Bzee9kY for passive taut mode (accessed on 1st Dec. 2023)).

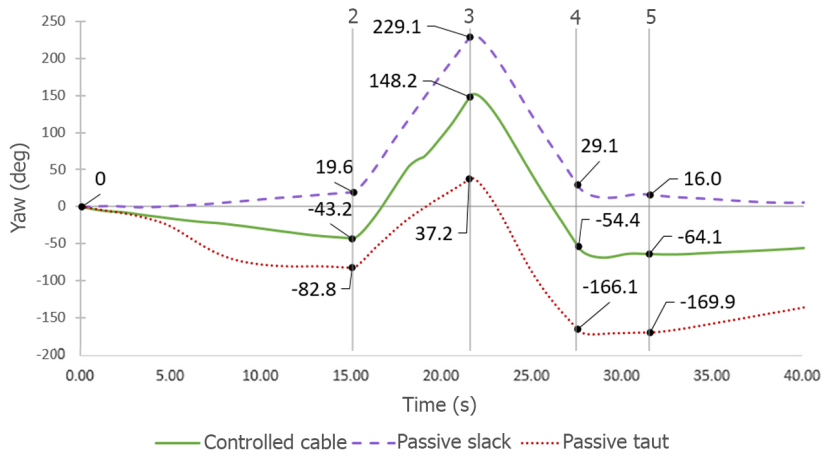

Figure 20. Comparison of the ROV yaw angle (measured with the embedded compass) along the curvilinear trajectory with or without cable control. The angle was initialized to 0^o at the beginning of the trajectories to facilitate their comparison. An increase in the angle represents a rotation to the right of the ROV.

The impact of these deviations is observed in Figure 21, in which the ROV paths in top view are shown for the three modes.

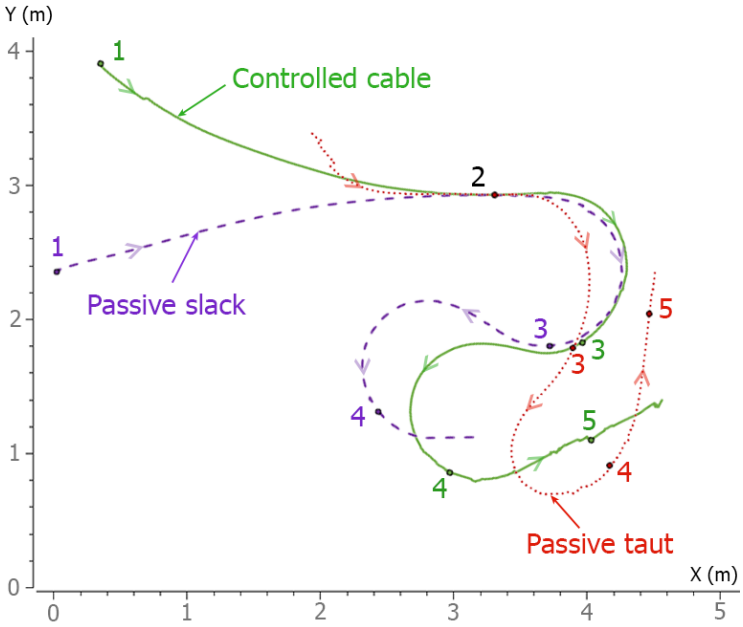

Figure 21. Comparison of the actual curvilinear path of the ROV in top view, measured by the *Qualisys* system, with or without cable control. These paths are superimposed on point 2 for easier comparison.

The distances traveled are quite similar for the controlled cable and the passive slack cable, whereas the turns are slightly different. The path of the ROV with the passive taut cable is completely distorted. The first rotation to the right (between points 2 and 3) is tightly confined, and the rotation to the left (between points 3 and 4) is quite irregular (much wider curvature in the middle than at the beginning and the end).

The experiments also showed there is effective control of the cable using the compliant buoy–ballast system, which keeps the cable in a semi-stretched configuration, and the delivered length is appropriately managed, preventing the creation of cable loops that can occur in passive slack mode and reducing the risks of snagging and tangles, considering that turns in passive taut mode can cause the cable to become entangled with the robot. The control mode generates slight tension in the cable, which is transmitted to the ROV and results in a minor deviation in the trajectory of the system, which can be avoided by fixing the cable closer to the ROV's center of gravity. In addition, the passive compliance system appears to improve the stability of the depth control of the ROV.

6. Conclusions

In this paper, a mechatronic solution for ROV deployment is introduced in which the length of the cable that connects the robot to the surface is automatically controlled. This solution consists of designing and setting up a balanced and compliant buoy–ballast system for the cable, which allows the cable feeder to be controlled using the readings from the flex sensor placed along a part of the cable near the ballast.

- The simulations and the experiments conducted with a BlueROV and a neutral cable demonstrated the validity of the concept. The steady-state model was used in the control loop to obtain a target distance between the buoys from the ROV speed command. The feeder appeared to react as expected with respect to the command speeds of the ROV.
- The shape of the cable was kept in a semi-stretched configuration during the experiments of linear and curved trajectories.
- This solution is easy to set up and can be useful in preventing the cable from pulling on the ROV, thus avoiding entanglement of the cable with its surroundings.

The aim for future developments will be to implement the cable feeder on a surface vehicle (USV). The measurement of the consumed current will help in estimating the cable

strain on the USV side. It will also be possible to equip the tether with strain sensors on the ROV side to increase the accuracy of closed-loop control with respect to the distance between buoys. Possible prospects include navigation synchronization between the ROV and the USV to optimize displacement of the vehicles in terms of power consumption and to increase seabed coverage in shallow waters.

Author Contributions: Conceptualization, methodology, writing, and data curation, O.T.; formal analysis and investigation, C.P.; project administration, supervision, validation, writing, formal analysis, review, and editing, C.A. and V.H. All authors have read and agreed to the published version of the manuscript.

Funding: This research was funded by the Provence-Alpes-Côte d'Azur (PACA) region for the *'Emploi jeunes doctorants'* (EJD) project, and the 3rd TransNational Access (TNA) H2020 European project related to EuMarineRobots.

Informed Consent Statement: Informed consent was obtained from all subjects involved in the study.

Data Availability Statement: No new data were created or analyzed in this study. Data sharing is not applicable to this article.

Acknowledgments: The authors greatly thank the CIRS lab (Underwater Robotics Research Center) in Girona, Spain, especially Pere Ridao and Guillem Vallicrosa Massaguer for their welcome and administrative and technical support during the week of experiments in the frame of the TNA project.

Conflicts of Interest: The authors declare no conflicts of interest.

Appendix A. Statics Analysis of the Buoy–Ballast System

The entire system is assumed to move at a constant velocity v driven by the ROV in the left–right direction. Assuming that all forces intersect at B_1, the compensation of forces exerted on the left buoy is calculated as

$$W_{buoy} + T_{B1}^{y} = 0 \quad \text{(A1)}$$

$$-F_{d}^{buoy} - T_1 + T_{B1}^{x} = 0 \quad \text{(A2)}$$

where T_{B1}^{x} and T_{B1}^{y} are the components of the force $\mathbf{T_{B1}}$ that is exerted by the cable portion B_1C onto the left buoy. F_{d}^{buoy} is the intensity of the drag force exerted by the fluid on the buoy. $T_1 > 0$ is the magnitude of the horizontal scalar force exerted by the cable that links the left buoy to the remote station.

Assuming that all forces intersect at B_2, the compensation of forces exerted on the right buoy is calculated as

$$W_{buoy} + T_{B2}^{y} = 0 \quad \text{(A3)}$$

$$-F_{d}^{buoy} + T_2 + T_{B2}^{x} = 0 \quad \text{(A4)}$$

where T_{B2}^{x} and T_{B2}^{y} are the components of the force $\mathbf{T_{B2}}$ that is exerted by the cable portion B_2C onto the right buoy. T_2 is the algebraic horizontal scalar force exerted by the cable that links the right buoy to the ROV. In the case of the figure, the intensity T_2 is positive since the ROV pulls on the cable to move from left to right.

Taking into account a drag force of intensity $F_{d}^{CB_1}$ and $F_{d}^{CB_2}$, resp., on the cable portions CB_1 and CB_2, the compensation of forces exerted on the ballast is

$$-W_{ballast} - T_{B1}^{y} - T_{B2}^{y} = 0 \quad \text{(A5)}$$

$$-F_{d}^{ballast} - F_{d}^{CB_1} - F_{d}^{CB_2} - T_{B1}^{x} - T_{B2}^{x} = 0 \quad \text{(A6)}$$

Equation (A5) is actually not useful since it was already set that $W_{ballast} = 2.W_{buoy}$, which can be found again using Equations (A1) and (A3).

In addition, the cable stiffness must be taken into account in the compensation of the efforts exerted on cable portions CB_1 and CB_2. Taking C as a reference point, the compensation of the moments of force and torques exerted on CB_1 is expressed as

$$\left[\mathbf{r_{CB_1}} \times (-\mathbf{T_{B1}}) + \frac{\mathbf{1}}{\mathbf{2}}\mathbf{r_{CB_1}} \times \mathbf{F_d^{CB_1}} + \mathbf{Tq_{B_1}^s} + \mathbf{Tq_{C,right}^s}\right].\mathbf{z} = \mathbf{0}$$

and on CB_2 as

$$\left[\mathbf{r_{CB_2}} \times (-\mathbf{T_{B2}}) + \frac{\mathbf{1}}{\mathbf{2}}\mathbf{r_{CB_2}} \times \mathbf{F_d^{CB_2}} + \mathbf{Tq_{B_2}^s} + \mathbf{Tq_{C,left}^s}\right].\mathbf{z} = \mathbf{0}$$

where $\mathbf{r_{CB_1}}$ and $\mathbf{r_{CB_2}}$ are the position vectors of B_1 and B_2, resp., with regard to C, and

- $\mathbf{Tq_{B_1}^s}$ is the cable bending torque exerted onto the branch B_1C at B_1, and $\mathbf{Tq_{B_2}^s}$ is the cable bending torque exerted onto the branch B_2C at B_2.
- $\mathbf{Tq_{C,right}^s}$ and $\mathbf{Tq_{C,left}^s}$ are the cable bending torques exerted by the right and left parts, resp., at C.

These torques are proportional to a bending stiffness coefficient named C_s. The equations above yield

$$\begin{aligned}
(T_{B1}^x + \frac{1}{2}.F_d^{CB_1}).\ell.\cos\theta_1 + T_{B1}^y.\ell.\sin\theta_1 + C_s\left[2(\frac{\pi}{2} - \theta_1) + (\frac{\pi}{2} + \theta_2)\right] &= 0 \\
(T_{B2}^x + \frac{1}{2}.F_d^{CB_2}).\ell.\cos\theta_2 + T_{B2}^y.\ell.\sin\theta_2 - C_s\left[2(\frac{\pi}{2} + \theta_2) + (\frac{\pi}{2} - \theta_1)\right] &= 0
\end{aligned}$$

The number of independent equations is therefore

$$\begin{aligned}
W_{buoy} + T_{B1}^y &= 0 \\
-F_d^{buoy} - T_1 + T_{B1}^x &= 0 \\
W_{buoy} + T_{B2}^y &= 0 \\
-F_d^{buoy} + T_2 + T_{B2}^x &= 0 \\
-F_d^{ballast} - F_d^{CB_1} - F_d^{CB_2} - T_{B1}^x - T_{B2}^x &= 0 \\
(T_{B1}^x + \frac{1}{2}.F_d^{CB_1}).\ell.\cos\theta_1 + T_{B1}^y.\ell.\sin\theta_1 + C_s\left[2(\frac{\pi}{2} - \theta_1) + (\frac{\pi}{2} + \theta_2)\right] &= 0 \\
(T_{B2}^x + \frac{1}{2}.F_d^{CB_2}).\ell.\cos\theta_2 + T_{B2}^y.\ell.\sin\theta_2 - C_s\left[2(\frac{\pi}{2} + \theta_2) + (\frac{\pi}{2} - \theta_1)\right] &= 0
\end{aligned}$$

Replacing T_{B1}^x, T_{B1}^y, T_{B2}^x, and T_{B2}^y in the last two equations yields

$$\begin{aligned}
T_{B1}^x &= F_d^{buoy} + T_1 \\
T_{B1}^y &= -W_{buoy} \\
T_{B2}^x &= -F_d^{ballast} - F_d^{CB_1} - F_d^{CB_2} - F_d^{buoy} - T_1 \\
T_{B2}^y &= -W_{buoy} \\
T_2 &= 2.F_d^{buoy} + F_d^{ballast} + F_d^{CB_1} + F_d^{CB_2} + T_1 \\
(F_d^{buoy} + T_1 + \frac{1}{2}.F_d^{CB_1}).\ell.\cos\theta_1 - W_{buoy}.\ell.\sin\theta_1 &= -C_s\left[2(\frac{\pi}{2} - \theta_1) + (\frac{\pi}{2} + \theta_2)\right] \\
-(F_d^{ballast} + F_d^{buoy} + T_1 + F_d^{CB_1} + \frac{1}{2}.F_d^{CB_2}).\ell.\cos\theta_2 - W_{buoy}.\ell.\sin\theta_2 & \\
= C_s\left[2(\frac{\pi}{2} + \theta_2) + (\frac{\pi}{2} - \theta_1)\right] &
\end{aligned}$$

References

1. Christ, R.; Wernli, R. *The ROV Manual a User Guide for Remotely Operated Vehicles*, 2nd ed.; Elsevier: Amsterdam, The Netherlands, 2014.
2. Khatib, O.; Yeh, X.; Brantner, G.; Soe, B.; Kim, B.; Ganguly, S.; Stuart, H.; Wang, S.; Cutkosky, M.; Edsinger, A.; et al. Ocean one: A robotic avatar for oceanic discovery. *IEEE Robot. Autom. Mag.* **2016**, *23*, 20–29.
3. Destelle, J.J.; Vallée, C. The MEUST infrastructure for neutrino astronomy. *Nucl. Instruments Methods Phys. Res. Sect. A Accel. Spectrometers Detect. Assoc. Equip.* **2013**, *725*, 227–229.
4. Capocci, R.; Dooly, G.; Omerdić, E.; Coleman, J.; Newe, T.; Toal, D. Inspection-Class Remotely Operated Vehicles—A Review. *J. Mar. Sci. Eng.* **2017**, *5*, 13.
5. Ajwad, S.A.; Iqbal, J. Recent Advances and applications of tethered robotic systems. *Sci. Int.* **2014**, *26*, 2045–2051.
6. Tortorici, O.; Anthierens, C.; Hugel, V.; Barthelemy, H. Towards active self-management of umbilical linking ROV and USV for safer submarine missions. *IFAC-PapersOnLine* **2019**, *52*, 265–270.
7. McLain, T.W.; Rock, S.M. Experimental Measurement of ROV Tether Tension. In Proceedings of the ROV '92, San Diego, CA, USA, 10-12 June 1992; p. 6.
8. Bevilacqua, L.; Kleczka, W.; Kreuzer, E. On the Mathematical Modeling of ROV'S. *IFAC Proc. Vol.* **1991**, *24*, 51–54.
9. Soylu, S.; Buckham, B.J.; Podhorodeski, R.P. Dynamics and control of tethered underwater-manipulator systems. In Proceedings of the OCEANS 2010 MTS/IEEE SEATTLE, Seattle, WA, USA, 20–23 September 2010; pp. 1–8.
10. Fang, M.C.; Hou, C.S.; Luo, J.H. On the motions of the underwater remotely operated vehicle with the umbilical cable effect. *Ocean Eng.* **2007**, *34*, 1275–1289.
11. Feng, Z.; Allen, R. Evaluation of the effects of the communication cable on the dynamics of an underwater flight vehicle. *Ocean Eng.* **2004**, *31*, 1019–1035.
12. Gay Neto, A.; de Arruda Martins, C. Structural stability of flexible lines in catenary configuration under torsion. *Mar. Struct.* **2013**, *34*, 16–40.
13. Coyne, J. Analysis of the formation and elimination of loops in twisted cable. *IEEE J. Ocean. Eng.* **1990**, *15*, 72–83.
14. Drumond, G.; Pasqualino, I.; Pinheiro, B.; Estefen, S. Pipelines, risers and umbilicals failures: A literature review. *Ocean Eng.* **2018**, *148*, 412–425.
15. Brignone, L.; Raugel, E.; Opderbecke, J.; Rigaud, V.; Piasco, R.; Ragot, S. First sea trials of HROV the new hybrid vehicle developed by IFREMER. In Proceedings of the OCEANS 2015—Genova, Genova, Italy, 18–21 May 2015; pp. 1–7.
16. Viel, C. Self-management of the umbilical of a ROV for underwater exploration. *Ocean Eng.* **2022**, *248*, 110695.
17. Frank, J.E.; Geiger, R.; Kraige, D.R.; Murali, A. Smart Tether System for Underwater Navigation and Cable Shape Measurement. U.S. Patent US8437979B2, 7 May 2013.
18. Duncan, R.G.; Froggatt, M.E.; Kreger, S.T.; Seeley, R.J.; Gifford, D.K.; Sang, A.K.; Wolfe, M.S. High-accuracy fiber-optic shape sensing. In Proceedings of the SPIE Smart Structures and Materials + Nondestructive Evaluation and Health Monitoring, San Diego, CA, USA, 18–22 March; p. 65301S.
19. Xu, C.; Chen, J.; Yan, D.; Ji, J. Review of Underwater Cable Shape Detection. *J. Atmos. Ocean. Technol.* **2016**, *33*, 597–606.
20. Xu, C.; Wan, K.; Chen, J.; Yao, C.; Yan, D.; Ji, J.; Wang, C. Underwater cable shape detection using ShapeTape. In Proceedings of the OCEANS 2016 MTS/IEEE Monterey, Monterey, CA, USA, 19–23 September 2016; pp. 1–4.
21. Banerjee, A.K.; Do, V.N. Deployment control of a cable connecting a ship to an underwater vehicle. *J. Guid. Control. Dyn.* **1994**, *17*, 1327–1332.
22. Zhao, C.; Thies, P.R.; Johanning, L. Investigating the winch performance in an ASV/ROV autonomous inspection system. *Appl. Ocean Res.* **2021**, *115*, 102827.
23. Raugel, E.; Opderbecke, J.; Fabri, M.; Brignone, L.; Rigaud, V. Operational and scientific capabilities of Ariane, Ifremer's hybrid ROV. In Proceedings of the OCEANS 2019—Marseille, Marseille, France, 17–20 June 2019.
24. Zhou, H.; Cao, J.; Yao, B.; Lian, L. Hierarchical NMPC–ISMC of active heave motion compensation system for TMS–ROV recovery. *Ocean Eng.* **2021**, *239*, 109834.
25. Lubis, M.B.; Kimiaei, M.; Efthymiou, M. Alternative configurations to optimize tension in the umbilical of a work class ROV performing ultra-deep-water operation. *Ocean Eng.* **2021**, *225*, 108786.
26. Laranjeira, M.; Dune, C.; Hugel, V. Catenary-based visual servoing for tether shape control between underwater vehicles. *Ocean Eng.* **2020**, *200*, 107018.
27. Tortorici, O.; Anthierens, C.; Hugel, V. A new flex-sensor-based umbilical-length management system for underwater robots. In Proceedings of the European Conference on Mobile Robotics, Coimbra, Portugal, 4–7 September 2023.